INTERNATIONAL JOURNAL FOR NUMERICAL METHODS IN FLUIDS
Int. J. Numer. Meth. Fluids 2002; **39**:485–496 (DOI: 10.1002/fld.283)

Numerical simulation for rotating internal weakly viscoelastic flows in rectangular ducts

A. L. de Bortoli*, M. Thompson and A. U. Zavaleta Calderon

Federal University of Rio Grande do Sul, Department of Pure and Applied Mathematics-PPGMAp, Bento Gonçalves 9500, 90501-900, Porto Alegre—RS, Brazil

SUMMARY

The present work develops a numerical method for the solution of rotating internal weakly viscoelastic flows in rectangular ducts for dimensionless parameters such as the Reynolds, Rossby and Weissenberg numbers, taken respectively in the intervals between 171 and 12 000, 0.047 and 1/12 and up to 1/10 000. It is shown that the usual counter-rotating double-vortex configuration of secondary flow breaks down with the increase of the Reynolds number (over the threshold of 171). For higher Reynolds numbers such as 7500 and 12 000 the secondary flow diffuses to the interior of the duct where it assumes a fully developed configuration and the transition to the turbulence structure is observed. The Sobolev norms increase almost proportionally to the increase of the Reynolds number, and play an essential role for more complex problems involving transition to turbulence modelling. Copyright © 2002 John Wiley & Sons, Ltd.

KEY WORDS: weakly viscoelastic; rotating flows; rectangular ducts; finite differences

1. INTRODUCTION

In this paper we present some computational results obtained for a model first introduced by Speziale [1], describing the flows of weakly viscoelastic incompressible fluids in rotating machinery with externally determined pressure gradient. In his paper, Speziale gave some numerical simulations for such a pressure driven flow through rectangular ducts subject to spanwise rotations, all at fairly low Reynolds numbers (up to 248). It was seen there that the secondary flows evidenced substantially lower frictional drag as compared with the Newtonian case, a striking nonlinear effect.

Since the model was obtained under fairly drastic approximations from the original Maxwell model, we discuss here numerical simulations by means of finite difference techniques in order to examine the persistence of this effect for higher Reynolds number. We observe at $Re = 12\,000$ a considerable growth of the secondary flow *vis á vis* the principal flow and an essential break down of the hypothesis of the model. Interestingly, the numerically calculated

*Correspondence to: A. L. de Bortoli, Department of Pure and Applied Mathematics, Federal University of Rio Grande do Sul, Bento Gonçalves 9500, 90501-900, Porto Alegre—RS, Brazil.

Received January 2001
Revised November 2001

Sobolev norms of the flow variables reflect the complexity of the flow. Such norms are useful as an input in the analytical theory developed by one of the authors [2] and in some preliminary results on nonlinear Galerkin approximations, described at the ICIAM 95 meeting, which will be described by the authors elsewhere in a more complete form.

It is worth noting that our simulations have been carried out for parameter values excluded from the range under which the global existence results in Reference [2] were established, although local results exist without such restrictions and as previously observed for higher Reynolds and Rossby numbers than those given in Reference [1].

2. THE MATHEMATICAL MODEL AND NUMERICAL ALGORITHM

The equations describing the model, obtained as an approximation from a Maxwell model for the fluid, in terms of nondimensional parameters, may be written in the following form:

$$\frac{\partial w}{\partial t} + u\frac{\partial w}{\partial x} + v\frac{\partial w}{\partial y} = C + R_e^{-1}\Delta w + 2R_o^{-1}u \tag{1}$$

$$\frac{\partial \zeta}{\partial t} + u\frac{\partial \zeta}{\partial x} + v\frac{\partial \zeta}{\partial y} = R_e^{-1}\Delta\zeta + 2W_e\left(\frac{\partial w}{\partial x}\frac{\partial}{\partial y}\Delta w - \frac{\partial w}{\partial y}\frac{\partial}{\partial x}\Delta w\right) + 2R_o^{-1}\frac{\partial w}{\partial y} \tag{2}$$

$$-\Delta\psi = \zeta \tag{3}$$

$$u = \frac{\partial \psi}{\partial y}, \quad v = -\frac{\partial \psi}{\partial x} \tag{4}$$

In the above equations, R_e is the Reynolds, R_o the Rossby, W_e the Weissenberg and C the dimensionless pressure number, where we recall that if W_0 is a velocity scale and S a length scale, then $R_e = [(W_0 S)/(v)]$, $Ro = [(W_0)/(\Omega S)]$, $C = [(\rho W_0^2)/(GS)]$ and $W_e = [(\lambda v)/(S^2)]$. Here ρ is the fluid density, v the kinematic viscosity ($v = \mu/\rho$), Ω the angular rotation and λ is the relaxation time involved in the weakly viscoelastic term. These nonlinear partial differential equations are subject to the following boundary conditions in the region $R = (0,\chi)\times(0,L)$ where $\chi = D/S$, $L = H/S$ are the aspect ratios related to the physical region $(0,D)\times(0,H)$.

$$\frac{\partial \psi}{\partial n} = \psi = 0, \quad w = 0$$

on

$$\Gamma = \partial\Omega = (0,\chi)\times(0,L)\cup(0,\chi)\times(0,L)$$

In the results reported here $\chi = 1$, $L = 8$.

Our basic finite difference approximation for the governing Equations (1)–(4) is given by

$$\frac{w_{i,j}^{t+\Delta t} - w_{i,j}}{\Delta t} = -u_{i,j}\frac{w_{i+1,j} - w_{i-1,j}}{2\Delta x} - v_{i,j}\frac{w_{i,j+1} - w_{i,j-1}}{2\Delta y} + C + {R_e}^{-1}[\Delta w]_{i,j} + 2{R_o}^{-1}u_{i,j} \tag{5}$$

$$\begin{aligned}\frac{\zeta_{i,j}^{t+\Delta t} - \zeta_{i,j}}{\Delta t} = {} & -u_{i,j}\frac{\zeta_{i+1,j} - \zeta_{i-1,j}}{2\Delta x} - v_{i,j}\frac{\zeta_{i,j+1} - \zeta_{i,j-1}}{2\Delta y} \\ & + R_e^{-1}\left[\frac{\zeta_{i-1,j} - 2\zeta_{i,j} + \zeta_{i+1,j}}{(\Delta x)^2} + \frac{\zeta_{i,j-1} - 2\zeta_{i,j} + \zeta_{i,j+1}}{(\Delta y)^2}\right] \\ & + 2W_e\left(\frac{w_{i+1,j} - w_{i-1,j}}{2\Delta x}\frac{[\Delta w]_{i,j+1} - [\Delta w]_{i,j-1}}{2\Delta y}\right. \\ & \left. - \frac{w_{i,j+1} - w_{i,j-1}}{2\Delta y}\frac{[\Delta w]_{i+1,j} - [\Delta w]_{i-1,j}}{2\Delta x}\right) \\ & + 2R_o^{-1}\left(\frac{w_{i,j+1} - w_{i,j-1}}{2\Delta y}\right)\end{aligned} \tag{6}$$

$$\psi_{i,j} = \frac{(\Delta x)^2(\Delta y)^2}{2[(\Delta x)^2 + (\Delta y)^2]}\left[\zeta_{i,j} + \frac{\psi_{i+1,j} + \psi_{i-1,j}}{(\Delta x)^2} + \frac{\psi_{i,j+1} + \psi_{i,j-1}}{(\Delta y)^2}\right] \tag{7}$$

$$u_{i,j} = \left(\frac{\psi_{i,j+1} - \psi_{i,j-1}}{2\Delta y}\right) \tag{8}$$

$$v_{i,j} = -\left(\frac{\psi_{i+1,j} - \psi_{i-1,j}}{2\Delta x}\right) \tag{9}$$

where

$$[\Delta w]_{i,j} = \frac{w_{i-1,j} - 2w_{i,j} + w_{i+1\,j}}{(\Delta x)^2} + \frac{w_{i,j-1} - 2w_{i,j} + w_{i,j+1}}{(\Delta y)^2} \tag{10}$$

with $i = 1, 2, \ldots, M$, $j = 1, 2, \ldots, N$, $n = 1, 2, \ldots, \Delta x\,\Delta y$ are the length in x and y directions, respectively, and Δt is the time step. Equations (5)–(10) are the complete finite difference formulation of the problem (1)–(4).

In order to obtain numerical solutions of high accuracy, the Runge–Kutta time-stepping scheme is chosen (see Reference [3]) while more than two stages are employed in order to extend its stability region. Since, for example, the classical fourth order Runge–Kutta method requires the evaluation of many coefficients and dissipative terms, which leads to storage

problems, we employ the following multistage scheme with low storage requirements

$$\begin{aligned}\vec{W}_{i,j}^{(0)} &= \vec{W}_{i,j}^{n} \\ \vec{W}_{i,j}^{(r)} &= \vec{W}_{i,j}^{(0)} - \alpha_r \Delta t \vec{R}_{i,j}^{(r-1)} \\ \vec{W}_{i,j}^{(n+1)} &= \vec{W}_{i,j}^{(r)}.\end{aligned} \tag{11}$$

where α_r are the Runge–Kutta time-stepping coefficients, and $\vec{R}_{ij}$ the residual vector.

Efficient three and five-stage schemes are obtained with the allocation of the following coefficients:

$$\alpha_1 = 1/2, \quad \alpha_2 = 1/2, \quad \alpha_3 = 1$$

$$\alpha_1 = 1/4, \quad \alpha_2 = 1/6, \quad \alpha_3 = 3/8, \quad \alpha_4 = 1/2, \quad \alpha_5 = 1$$

A three-stage scheme is adopted which has been seen to be appropriate when solving incompressible fluid flow problems. In the general case of a nonuniform mesh, in terms of the Courant–Friedrich–Lewy (CFL) number the time interval satisfies the following condition (see Reference [4]):

$$\Delta t_{i,j} = \mathrm{CFL}\, \frac{V_{i,j}}{\lambda_{i,j}^{i} + \lambda_{i,j}^{j}}$$

where V_{ij} is the cell volume and λ_{ij} the spectral ratios of the Jacobian matrix. The superposition of generalized CFL and Neumann conditions was adopted here following the indication made by Speziale and results in the condition [1].

$$\Delta t_{i,j} \leqslant \left[2\nu \left(\frac{1}{\Delta x^2} + \frac{1}{\Delta y^2} \right) + \frac{|u|_{\max}}{\Delta x} + + \frac{|v|_{\max}}{\Delta y} \right]^{-1}$$

The flux vector $\vec{R}_{ij}$ is approximated in the following way for the second Runge–Kutta time-step, Equation (5), for example

$$\begin{aligned}R_{i,j}^{(2)} = \Bigg[& -u_{i,j} \frac{w_{i+1,j} - w_{i-1,j}}{2\Delta x} - v_{i,j} \frac{w_{i,j+1} - w_{i,j-1}}{2\Delta y} \\ & + C + Re^{-1} \left(\frac{w_{i-1,j} - 2w_{i,j} + w_{i+1,j}}{(\Delta x)^2} \right. \\ & \left. + \frac{w_{i,j-1} - 2w_{(i,j)} + w_{i,j+1}}{(\Delta y)^2} \right) + 2Ro^{-1} u_{i,j} \Bigg]^{(2)}\end{aligned} \tag{12}$$

Boundary conditions are specified using the no-slip condition for velocity and second-order approximations for the axial vorticity ζ, respectively. They can be written in the following

form.

$$\begin{aligned}\zeta_{0,j}&=\frac{8\psi_{i,j}-\psi_{2,j}}{2(\Delta x)^2}\\ \zeta_{M,j}&=\frac{8\psi_{M-1,j}-\psi_{M-2,j}}{2(\Delta x)^2}\\ \zeta_{i,1}&=\frac{8\psi_{i,1}-\psi_{i,2}}{2(\Delta y)^2}\\ \zeta_{i,N}&=\frac{8\psi_{i,N-1}-\psi_{i,N-2}}{2(\Delta y)^2}\end{aligned} \tag{13}$$

The initial conditions correspond to the case where $R_o \to \infty$ and $W_e \to 0$ (no rotation and Newtonian fluid) which means that, $\zeta = \psi = 0$ and w is the solution of the Poisson equation

$$C + R_e^{-1}\Delta w = 0 \tag{14}$$

This corresponds to the spin-up of the fully developed duct flow and to the way that experiments on rotating duct flows are usually conducted (see Speziale [1]).

3. NUMERICAL RESULTS

Equations (1) to (4) are solved numerically using the finite difference explicit Runge–Kutta scheme as described by Equations (5) to (10). The numerical algorithm is second-order accurate $(\Delta x^2, \Delta t^2)$ in space and time.

The numerical simulations presented here were conducted in a 1:8 rectangular duct using a mesh of 16×128. In each case, we prescribe the longitudinal pressure gradient, Reynolds, Rossby and Weissenberg numbers.

Figure 1(a) and (b) shows the streamlines computed for Reynolds number equal to $R_e = 171$ and $R_e = 248$, respectively, with $R_o = 0.047$, $G = 2 \times 10^{-4}$ lb ft^{-3} and $\Omega = 0.005$ rad s^{-1}. A comparison of these results with the ones obtained by Speziale shows good agreement between these solutions.

It is shown that the usual counter-rotating double-vortex configuration appears in the secondary flow, where the length scale of the vortices are of the order of the width of the duct, for $R_e = 171$. However, as the Reynolds number increases to 248, the double-vortex configuration breaks down into eight vortices almost symmetric relative to the horizontal centerline axis. Further increase of the Reynolds number to 5000 tends to produce eight equal and symmetrical vortices showing a flow configuration stable in the interior of the channel. There is no doubt that this flow is real, since the same results were obtained when the grid was refined with the time-step reduced and when the initial condition was changed during the calculation. It is also important to observe that R_o is relatively small in this situation.

Figure 2 shows the streamlines and the principal flow computed for $R_e = 500$, $R_o = 1/12$ and $C = 0.01$. The streamlines denote the secondary flow due to rotation of the duct. It seems clear from the pictures that in the low Reynolds number Figure 1(a) case, the roll-cells of axial vorticity are less numerous than in the high Reynolds number case. It is quite clear that the secondary flow start as a double-vortex configuration that is strongly compressed against the upper and lower walls of the duct. As the Reynolds number increases, this secondary

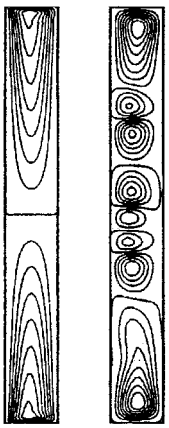

Figure 1. Streamlines for $R_o = 0.047$, $G = 2 \times 10^{-4}$ lb ft^{-3} and $\Omega = 0.005$ rad s^{-1}; (a) $R_e = 171$, (b) $R_e = 248$.

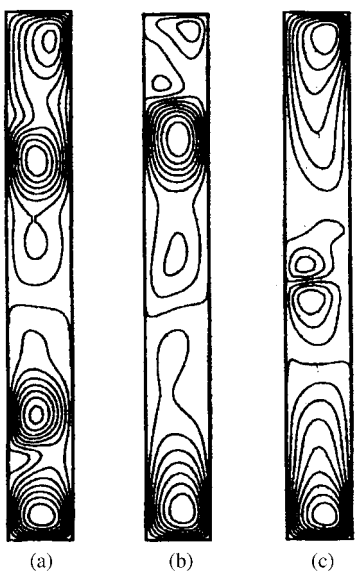

Figure 2. Streamlines for $R_e = 500$, $R_o = 1/12$, $C = 0.01$; (a) $W_e = 0$, (b) $W_e = 1/50\,000$, (c) $W_e = 1/10\,000$.

flow diffuses [5] to the interior of the duct where it assumes a fully developed configuration (Figure 2). As the Rossby number is of order $1/12$ the cell instabilities are big, but not enough to turn the structure completely unstable (turbulent). The magnitude of the secondary flow relative to the axial flow near the horizontal centerline is substantially larger than for the small Reynolds number.

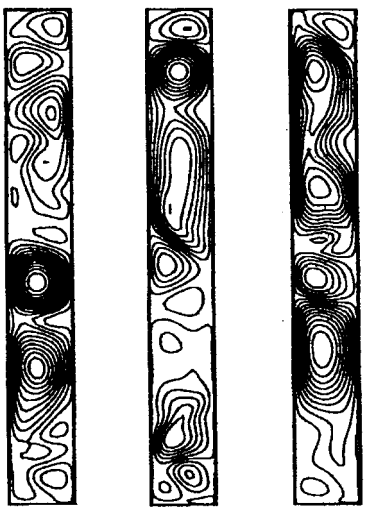

Figure 3. Streamlines for $R_e = 5000$, $R_o = 1/12$, $C = 0.0001$; (a) $W_e = 0$, (b) $W_e = 1/50\,000$, (c) $W_e = 1/10\,000$.

Figure 3 shows the streamlines and the principal flow for $R_e = 5000$, $R_o = 1/12$ and $C = 0.0001$. Unfortunately, a direct comparison cannot be made between the numerical values and experimental ones because there is a notable lack of experimental data on this problem. Numerical results show that the axial velocity along the horizontal centerline of the duct is highly asymmetric and a substantial decrease of the principal flow is observed. In the numerical experiments it was necessary to reduce the dimensionless pressure number C to 0.0001. For greater values such as 0.01 the numerical procedure was unstable. It is easy to understand this effect considering a given axial flow that is subjected to a continuous increase in the angular velocity Ω; the flow tends to be unstable and, consequently, the convective terms become less dominant.

Increasing again the Reynolds number to 7500 for the same parameters as for $Re = 5000$, a still more complex flow configuration is observed, as shown in Figure 4. For both cases the Weissenberg number is varied between 0 and $1/10\,000$. The flow configuration (streamlines) after 50 000 iterations are seen to be different in the presence of viscoelasticity, however, as will be mentioned below, the Sobolev norms were almost the same.

In order to better visualize the flow behaviour for Reynolds between 500 and 12 000, Figures 5 and 6 show the streamlines and the vector field for this flow situation. The dimensionless pressure number C used to obtain the solution for $Re = 12\,000$ was equal to 0.0000001 because bigger values such as 0.0001 were not adequate in order to obtain a stable numerical code.

Through observation of Figure 6 it is easy to identify that an increase of vortices number as well as a decrease in their size is obtained when there is an increase in the Reynolds number. Probably the difficulties observed to obtain numerical results for even higher Reynolds numbers is associated with this behaviour. All big vortices tend to break down and the flow structure

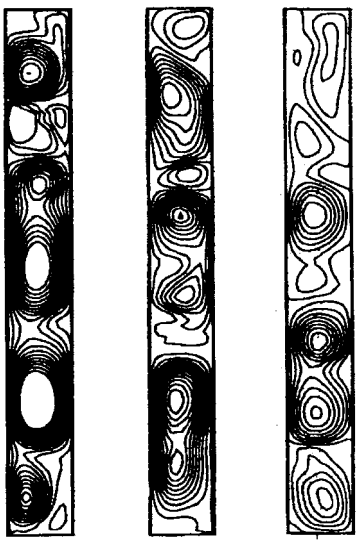

Figure 4. Streamlines for $R_e = 7500$, $R_o = 1/12$, $C = 0.0001$; (a) $W_e = 0$, (b) $W_e = 1/50\,000$, (c) $W_e = 1/10\,000$.

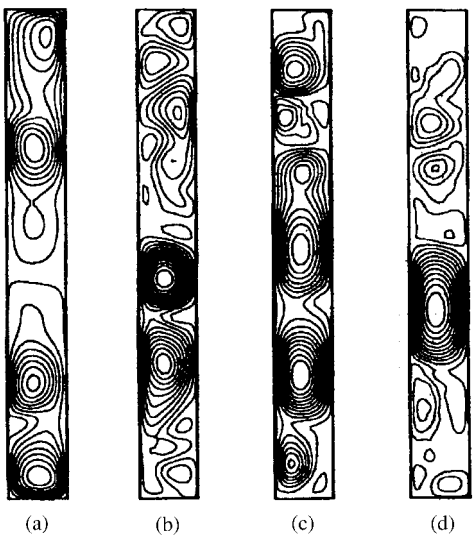

Figure 5. Streamlines for $W_e = 0$, $R_o = 1/12$; (a) $R_e = 500$, $C = 0.01$, (b) $R_e = 5000$, $C = 0.0001$, (c) $R_e = 7500$, $C = 0.0001$, (d) $R_e = 12\,000$, $C = 0.0000001$.

starts to be very complex. Figure 6 helps to clarify the vortices behaviour that appear for these flow situations.

Clearly, in order to obtain results for higher Reynolds numbers than the ones presented here it is necessary to use more careful spatial and time approximations which make the numerical

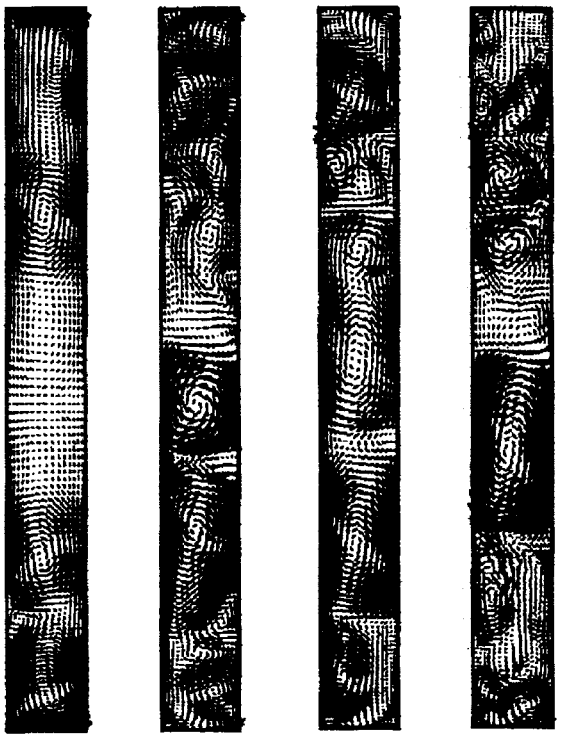

Figure 6. Vector field for $W_e = 0$, $R_o = 1/12$; (a) $R_e = 500$, $C = 0.01$, (b) $R_e = 5000$, $C = 0.0001$, (c) $R_e = 7500$, $C = 0.0001$, (d) $R_e = 12\,000$, $C = 0.0000001$.

code more sophisticated and consequently more expensive. It takes about 25 min to generate the present solutions on an Silicon Graphics Origin 200 of our laboratory.

Subsequently, the Sobolev norms for variables w, ζ and ψ were analysed for the same flow situations presented in Figures 3, 4 and 5. Figure 7 shows the Laplacian of w for $R_e = 7500$, $R_o = 1/12$ and $C = 0.0001$. The Weissenberg number is varied between 0 and $1/10\,000$ in the simulations described in Figure 7(a), (b) and (c), respectively. Their mean values in both cases are almost the same, however their frequencies start to be small with the increase of the Weissenberg number, as can be seen in Equation (2).

A comparison between the Laplacian norms of w, ψ and ζ are presented in Figures 8–10. Figure 8 compares the w Sobolev norms for Reynolds numbers between 500 and 12 000. Their mean value increase with the increase of the Reynolds number. Results obtained for $Re = 500$ and $C = 0.01$ have the same behaviour, however the mean value tends to be bigger because of the increase of the dimensionless parameter C. For Reynolds 12 000 and very small C values the norms and their frequencies start to grow considerably.

Probably the increase of the Reynolds number will turn the numerical code unstable due to the breakdown of this structure. The same behaviour is observed for the other norms, as shown in Figures 9 and 10. However, the magnitudes of w and ζ are two orders greater than

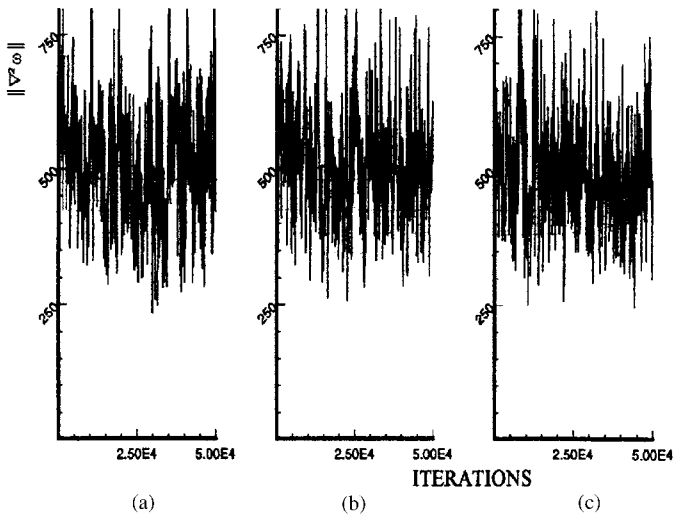

Figure 7. w Sobolev norms for $R_e = 7500$, $R_o = 1/12$ and $C = 0.0001$; (a) $W_e = 0$, (b) $W_e = 1/50\,000$, (c) $W_e = 1/10\,000$.

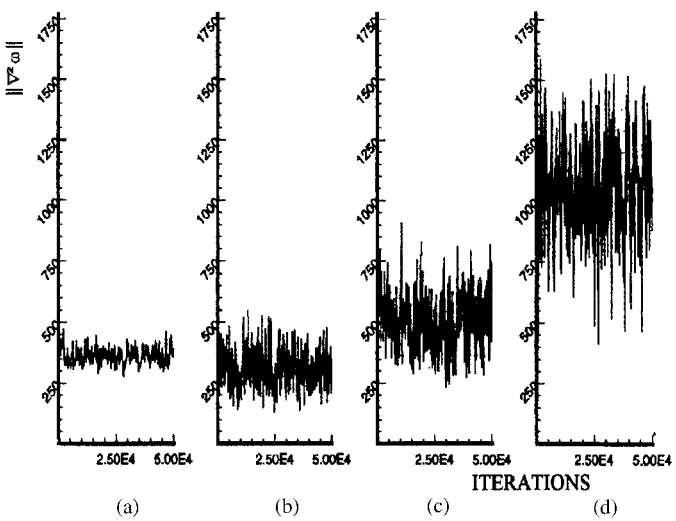

Figure 8. w Sobolev norms for $W_e = 0$ and $R_o = 1/12$; (a) $R_e = 500$, $C = 0.01$, (b) $R_e = 5000$, $C = 0.0001$, (c) $R_e = 7500$, $C = 0.0001$, (d) $R_e = 12\,000$, $C = 0.0000001$.

for ψ. The higher nonlinearity of the flow behaviour is apparent when analysing the results, for $R_e = 5000$ as well as $R_e = 12\,000$. This is an indication of why a complete mathematical analysis of the Navier–Stokes is still a challenge; moreover, the numerical results presented here can help us to better understand these difficulties.

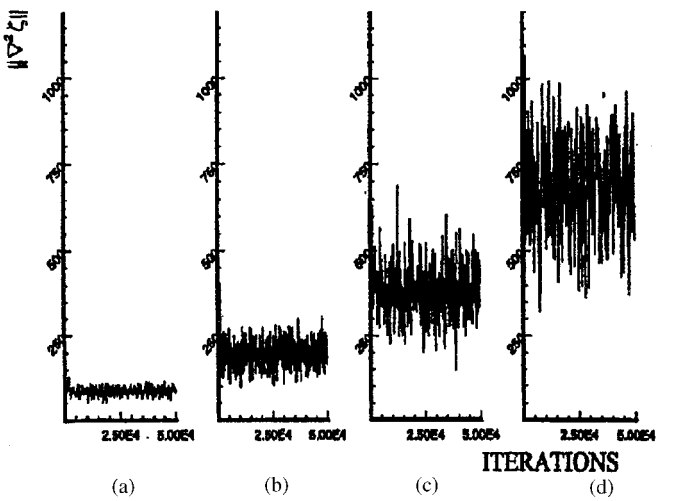

Figure 9. ζ Sobolev norms for $W_e = 1/50\,000$ and $R_o = 1/12$; (a) $R_e = 500,\ C = 0.01$, (b) $R_e = 5000$, $C = 0.0001$, (c) $R_e = 7500,\ C = 0.0001$, (d) $R_e = 12\,000,\ C = 0.0000001$.

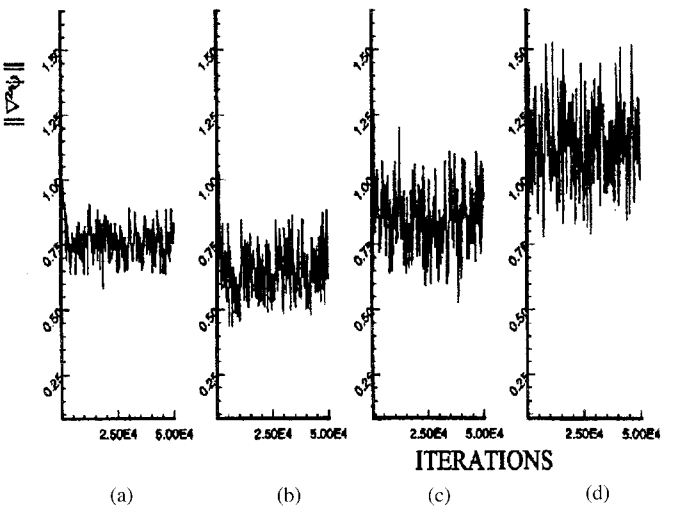

Figure 10. ψ Sobolev norms for $W_e = 0$ and $R_o = 1/12$; (a) $R_e = 500,\ C = 0.01$, (b) $R_e = 5000$, $C = 0.0001$, (c) $R_e = 7500,\ C = 0.0001$, (d) $R_e = 12\,000,\ C = 0.0000001$.

Simulations have been carried out for Reynolds numbers of the order of 12 000 where it is seen that an essential breakdown occurs at the underlying hypotheses of the model, $[(|u|)/(|w|)] \ll 1$, $[(|v|)/(|w|)] \ll 1$, while experimental results and simulations for the Navier–Stokes equations with rotation may be seen in the literature for bulk Reynolds number up to 30 000. However, as might be suspected, even using first order approximations, as in the

model of Speziale, it is necessary to treat an extension of the model which is strictly three dimensional. This case involves markedly more complicated nonlinear interactions.

4. CONCLUSIONS

It is shown that the usual counter-rotating double-vortex configuration for the secondary flow occurs for the aspect ratio 1:8 for a rectangular duct. However, as the rotation rate is substantially increased, this double-vortex configuration breaks down into an asymmetric of some counter rotating vortices. It is obvious that the Coriolis term $2\Omega[(\partial w)/(\partial y)]$, which acts as an axial vorticity source term, is the driving mechanism for the creation of secondary flow in a rotating duct. A decrease in the rotation rate leads to a restabilization of the secondary flow into a slightly deformed double-vortex configuration (see Reference [6]).

The magnitude of the secondary flow relative to the axial flow near the horizontal centerline of the 8:1 duct is substantially larger for the weak-to-moderate rotation case. It is quite clear that the asymmetry of the axial-velocity profiles along the horizontal centerline of the duct is a consequence of the convective terms. Besides, the principal velocity profiles indicate that velocities near the inner wall are greater than at the outer wall [7].

In conclusion, the numerical results obtained here indicate that there are many interesting physical phenomena associated with laminar and transitional flows in rotating rectangular ducts that are until now not totally understood. This understanding is essential if real progress is to be made for more complex problems involving turbulence whose applications in the area of turbomachinery are obvious, such as for centrifuges and turbines.

REFERENCES

1. Speziale CG. Numerical solutions of rotating flows, in large scale computations in fluid mechanics. *Lectures in Applied Mathematics*. AMS, Providence: Rhode Island, 1985; 261–288.
2. Rubio O, Thompson M. Hausdorff dimension of functionally invariant sets for rotating internal weakly viscoelastic fluids. *Nonlinear Analysis*, *Theory and Applications* 1998; **32**(2):201–223.
3. Jameson A, Schmidt W, Turkel E. Numerical solution of the Euler equations by finite volume methods using Runge–Kutta time-stepping schemes. *AIAA Journal* 1981; 81–1259.
4. Blazek J. Verfahren zur Beschlenunigung der Lösung der Euler-und Navier–Stokes Gleichungen bei Stationärem Über-und Hyperschall-strömungen. PhD Thesis, University of Braunschweig, 1994.
5. Johnston JP, Lezius DK. Roll-cell instabilities in rotating laminar and turbulent channel flows. *Journal of Fluid Mechanics* 1976; **77**:153–175.
6. Speziale CG, Thangam S. Numerical study of secondary flows and roll-cell instabilities in rotating channel flow. *Journal of Fluid Mechanics* 1983; **130**:377–395.
7. Speziale CG. Instabilities of the Taylor–Proudman theorem for rotating non-Newtonian fluids. *Proceedings of 12th. South Eastern Conference on Theoretical and Applied Mechanics*, 1984, vol. 11, pp. 3–9.

